




Cite this: *Biomater. Sci.*, 2018, **6**, 2110

## Noninvasive rapid bacteria-killing and acceleration of wound healing through photothermal/photodynamic/copper ion synergistic action of a hybrid hydrogel†

Mu Li,<sup>a</sup> Xiangmei Liu,<sup>\*a</sup> Lei Tan,<sup>a</sup> Zhenduo Cui,<sup>b</sup> Xianjin Yang,<sup>b</sup> Zhaoyang Li,<sup>b</sup> Yufeng Zheng,<sup>c</sup> Kelvin Wai Kwok Yeung,<sup>d</sup> Paul K. Chu<sup>e</sup> and Shuilin Wu<sup>†</sup> <sup>\*a,b</sup>

Bacterial infection often delays healing of wounded tissues and so it is essential to improve the antibacterial efficiency *in situ*. In this work, a hybrid hydrogel composed of 3-(trimethoxysilyl)propyl methacrylate (MPS, 97%) and mesoporous silica (mSiO<sub>2</sub>) modified CuS nanoparticles (NPs) is synthesized by radical polymerization. The materials possess excellent and controllable photothermal and photodynamic properties under 808 nm near-infrared (NIR) light irradiation as well as an antibacterial efficacy of 99.80% and 99.94% against *Staphylococcus aureus* and *Escherichia coli* within 10 min, respectively. The excellent performance stems from the combined effects of hyperthermia, radical oxygen species, and released copper ions produced during NIR irradiation of CuS NPs. Moreover, the released copper ions stimulate fibroblast proliferation and angiogenesis and the intrinsic volume transition of the hydrogel composed of *N*-isopropylacrylamide (NIPAAm) and acrylamide (AAm) controls the release rate of copper ions during NIR light irradiation leading to both antibacterial effects and skin tissue regeneration.

Received 5th May 2018,  
Accepted 18th May 2018

DOI: 10.1039/c8bm00499d

rsc.li/biomaterials-science

### 1. Introduction

Bacterial infectious diseases are responsible for one third of the global mortality.<sup>1,2</sup> For example, *Staphylococcus aureus* (*S. aureus*) can cause local purulent infection, pneumonia, septicemia, and other systemic infections and has become the most frequent cause of skin and soft tissue infection.<sup>3,4</sup> Skin tissues play the vital protective role against the external environment<sup>5,6</sup> and it is critical to accelerate the healing of damaged skin tissues while simultaneously avoiding bacterial infection. Currently, therapies based on antibiotics are the

most common methods to treat infection but overuse of antibiotics has led to bacterial resistance and even occurrence of superbacteria.<sup>7</sup> Silver NPs are considered broad spectrum antibacterial agents but besides the toxicity of silver NPs at higher concentrations,<sup>8</sup> bacteria can also develop resistance against them.<sup>9</sup> Furthermore, antibacterial treatments typically take a long time during which bacteria can mutate and evolve and therefore, it is imperative that bacteria are killed in a short time.

Photothermal therapy (PTT) or photodynamic therapy (PDT) induced by light irradiation is effective in killing bacteria as a non-resistant and minimally invasive process.<sup>10–13</sup> The use of UV-Vis irradiation to kill bacteria may not be desirable *in vivo* because of its damage to biological tissues and its absorption by tissues. On the other hand, NIR light ( $\lambda = 700–1100$  nm) which has relatively small absorption and scattering coefficients in biological tissues is more preferred in clinical applications.<sup>14–17</sup> Although NIR photothermal conversion agents such as indocyanine green dye,<sup>18</sup> carbon nanotubes,<sup>19</sup> and metal nanostructures including gold nanospheres,<sup>20</sup> gold nanorods,<sup>21</sup> gold nanocages,<sup>22</sup> as well as multifunctional gold nanoshells<sup>23</sup> have been investigated for PTT, practical biomedical applications are limited due to the small photothermal conversion efficiency or high cost.<sup>24</sup> Recently, semiconducting CuS NPs have emerged as promising photothermal agents (PTAs) on account of their intrinsic NIR region absorption, efficient heat generation,<sup>25–27</sup> low cost, biodegrad-

<sup>a</sup>Hubei Collaborative Innovation Center for Advanced Organic Chemical Materials, Ministry-of-Education Key Laboratory for the Green Preparation and Application of Functional Materials, Hubei Key Laboratory of Polymer Materials, School of Materials Science & Engineering, Hubei University, Wuhan 430062, China. E-mail: liuxiangmei1978@163.com

<sup>b</sup>School of Materials Science & Engineering, Tianjin University, Tianjin 300072, China. E-mail: shuilin.wu@gmail.com, shuilinwu@tju.edu.cn

<sup>c</sup>State Key Laboratory for Turbulence and Complex System and Department of Materials Science and Engineering, College of Engineering, Peking University, Beijing 100871, China

<sup>d</sup>Department of Orthopaedics & Traumatology, Li Ka Shing Faculty of Medicine, The University of Hong Kong, Pokfulam, Hong Kong 999077, China

<sup>e</sup>Department of Physics and Department of Materials Science and Engineering, City University of Hong Kong, Tat Chee Avenue, Kowloon, Hong Kong 999077, China

† Electronic supplementary information (ESI) available. See DOI: 10.1039/c8bm00499d

ability,<sup>28</sup> as well as synthetic simplicity on the industrial scale. CuS NPs can be used as photosensitizers in PTT but also generate reactive oxygen species (ROS) in PDT under NIR irradiation.<sup>29,30</sup> Therefore, this property can be exploited because CuS NPs may provide enhanced antibacterial efficacy under NIR irradiation. In addition, Cu ions have been demonstrated to promote wound healing due to the stimulation effects on proliferation and angiogenesis of cells.<sup>31–33</sup> Hence, a CuS NP-based system may offer antibacterial ability and accelerate wound healing at the same time. However, it has been shown that Cu ions released from the NPs affect the cell viability at high concentrations<sup>34</sup> and so controllable release of Cu ions instead of burst release must be accomplished. In addition, direct contact between Cu-containing NPs and wounds may produce inflammation in skin tissues<sup>35</sup> and CuS NPs administered as powders can easily detach from wounds as well.

Maintaining a moist environment around the wound facilitates wound healing<sup>36–38</sup> and because of the large water content, hydrogels have been used as wound-dressing materials to provide a moist environment for wound healing.<sup>10,39</sup> Hydrogels, which are three-dimensional (3D) networks composed of cross-linked hydrophilic polymer chains having large pore size and volume as well as specific surface area,<sup>40</sup> can provide the mechanical support for NPs. The moisture-retaining materials not only keep cells viable enabling them to release growth factors, but also may accommodate living cells and stimulate proliferation.<sup>37,41</sup> In this work, a CuS NP embedded hydrogel is designed and prepared to achieve great antibacterial activity as illustrated in Scheme 1. Fig. 1a

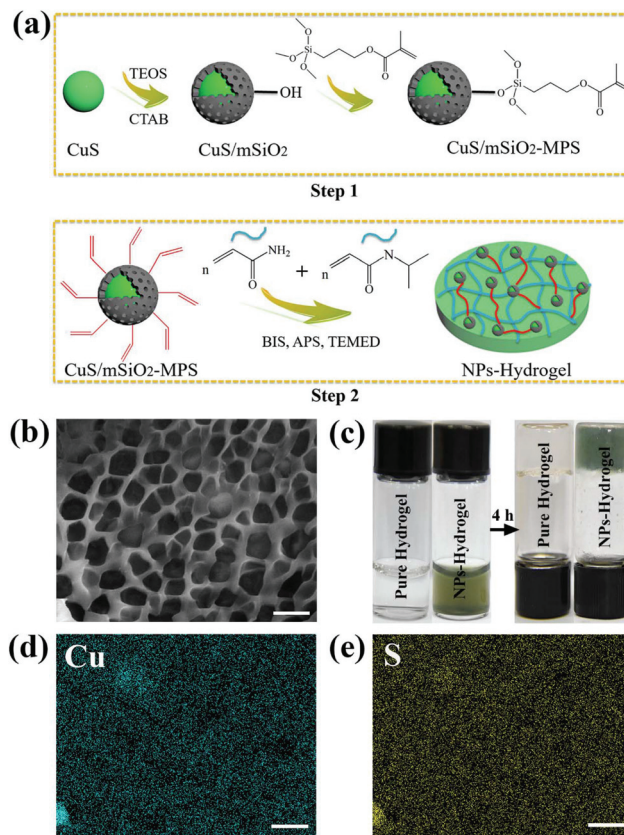
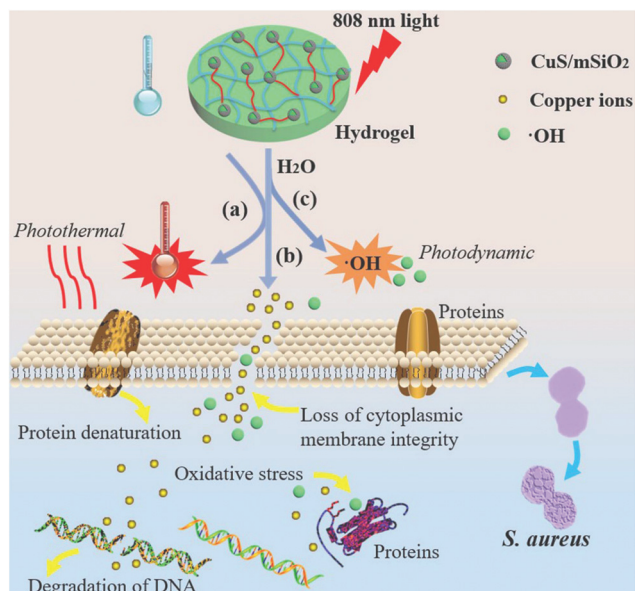


**Fig. 1** (a) Schematic illustration of the synthetic route of CuS/mSiO<sub>2</sub>-MPS/poly(NIPAAm-co-AAm) hydrogel. (b) SEM image of the dispersed CuS NPs in NPs-Hydrogel derived from radical polymerization. Scale bar, 5  $\mu$ m. (c) Photographs of the sol and gel states before or after radical polymerization for 4 h. (d, e) EDS elemental maps (Cu in green, S in yellow) of the NPs-Hydrogel. Scale bar, 5  $\mu$ m.



**Scheme 1** Schematic illustration of the bacteria killing processes with the hybrid hydrogel under 808 nm NIR light irradiation. (a) NIR light is absorbed and converted into heat. (b) The release of Cu ions formed by dissociation of ions from the CuS NPs. (c) The production of hydroxyl radicals ( $\cdot$ OH) through a reaction between free carriers and water molecules under NIR light.

illustrates the fabrication process of the nanocomposite hydrogels (NPs-Hydrogels) which will be described in more detail later. Although CuS-based NPs have been proposed as PTAs in antibacterial therapy, simultaneous wound healing has not been reported for CuS NPs combined with hydrogels. By taking advantage of the photothermal and photodynamic effects of CuS, angiogenesis of Cu ions, and moist conditions, the materials boast antibacterial activity and tissue regeneration capability at the same time. Moreover, the hydrogel based on NIPAAm and AAm undergoes volume conformation in response to small variations in temperature at a lower critical solution temperature (LCST)<sup>42</sup> and the volume transition triggered by hyperthermia under NIR light irradiation is demonstrated to control the release rate of Cu ions.

## 2. Experimental section

### 2.1 Synthesis of CuS/mSiO<sub>2</sub>-MPS NPs

The CuS NPs were prepared by a previously reported method with slight modification. 0.6 mmol of CuCl<sub>2</sub>·2H<sub>2</sub>O and 0.408 mmol of trisodium citrate dihydrate (C<sub>6</sub>H<sub>5</sub>Na<sub>3</sub>O<sub>7</sub>·2H<sub>2</sub>O,

Na<sub>3</sub>Cit) were mixed with 180 mL of deionized water in a three-necked bottle under stirring and then 20 mL of Na<sub>2</sub>S·9H<sub>2</sub>O (30 mmol L<sup>-1</sup>) was added drop by drop. The solution turned dark brown after stirring for 5 min at room temperature and was heated to 90 °C for 15 min. The solution was stored in ice water prior to use. 2.1 g of hexadecyltrimethylammonium bromide (CTAB) were dissolved in the CuS NP dispersion obtained from the last step and heated to 40 °C for 2 h under stirring. 9 mL of ethanol and 300 μL of NaOH (30 mg mL<sup>-1</sup>) were added and 300 μL of ethyl silicate (TEOS) were dropped into this mixture. After stirring at 40 °C for 1.5 h, the CuS/SiO<sub>2</sub> NPs were then collected by centrifugation (12 000 rpm for 10 min) and washed three times with ethanol. To remove the template of CTAB by ion exchange, the products were dispersed in the ethanol solution with NH<sub>4</sub>NO<sub>3</sub> (150 mL, 10 mg mL<sup>-1</sup>) and stirred at 50 °C for 2 h. The CuS/mSiO<sub>2</sub> NPs were rinsed three times with ethanol and collected by centrifugation. To further functionalize the surface of the CuS/mSiO<sub>2</sub> NPs with carbon-carbon double bonds, 50 mg of the microspheres were dispersed in 140 mL of ethanol and 1 mL of MPS was added to the dispersion. After stirring at 30 °C for 48 h, the microspheres (CuS/mSiO<sub>2</sub>-MPS) were washed with ethanol several times and collected by centrifugation.

## 2.2 Synthesis of the nanocomposite hydrogels

The nanocomposite hydrogels were prepared by conventional polymerization according to the previously reported method. A molar ratio of 95 : 5 (NIPAAm : AAm) was adopted to fabricate the NPs-Hydrogels by adding 0.4 g of NIPAAm (98%, recrystallized with hexane), 0.013 g of AAm, 8 mg of *N,N'*-methylenebis(acrylamide) (BIS, 99%), and 5 mL of deionized water containing various concentrations of CuS/mSiO<sub>2</sub>-MPS NPs (CH1: 0 mg mL<sup>-1</sup>, CH2: 0.5 mg mL<sup>-1</sup>, CH3: 1 mg mL<sup>-1</sup>, and CH4: 1.5 mg mL<sup>-1</sup>) to a beaker under stirring to form the primary polymer solution. The solution was purged with N<sub>2</sub> for 10 min and 4 mg of ammonium persulfate (APS) and 16 μL of *N,N,N',N'*-tetramethylethylenediamine (TEMED, 99%) were rapidly added. Polymerization proceeded for 4 h at room temperature and then the hydrogels were immersed in distilled water at room temperature for 24 h. The water was refreshed every 3 h in order to allow the unreacted chemicals to leach out and finally, the samples were obtained by vacuum freeze-drying.

## 2.3 Characterization

The morphology and size of the CuS NPs were characterized by transmission electron microscopy (TEM, Tecnai G20, FEI, USA) and selected-area electron diffraction (SAED). The morphology and elemental concentrations of the hydrogels were determined on a scanning electron microscope equipped with energy-dispersive X-ray spectrometry (EDS) (SEM, JSM-6510LV, JEOL, Japan). The surface chemical composition of the NPs was determined by X-ray photoelectron spectroscopy (XPS) (ESCALAB 250Xi, Thermo Scientific, USA) and Fourier transform infrared (FTIR, NICOLET iS10) spectroscopy was employed to identify the surface functional chemical groups of the samples. To determine the phase structure of the hydro-

gels, the samples were analyzed by X-ray diffraction (XRD, D8A25, Bruker, Germany) in the continuous mode with  $2\theta$  from 20° to 80° and a step size of 0.02°. Inductively-coupled plasma atomic emission spectrometry (ICP-AES) was carried out on an Optimal 8000 (PerkinElmer, USA) to determine the concentration of the released copper ions. The extinction spectra were acquired from the hydrogels on a UV-Vis spectrophotometer (SpectraMax I3, Molecular Devices) and a contact angle instrument (Powereach, JC2000D2) was used to monitor the changes in the surface wettability of the hydrogels during light irradiation. Differential scanning calorimetry (DSC, TA Q2000) was used to measure the lower critical solution temperature of the hydrogel as the temperature was increased from 25 °C to 45 °C at a rate of 1 °C min<sup>-1</sup>. A light source (808 nm, LOS-BLD-0808) was utilized to produce the photothermal and photodynamic effects.

## 2.4 Photothermal effects under 808 nm laser irradiation

The photothermal conversion efficiency of the hydrogels was measured according to the reference reported previously. The NIR laser light (808 nm) with a power of 1.55 W (power density 2 W cm<sup>-2</sup>) was focused to a spot size of 1 cm. The hydrogels (CH1, CH2, CH3, and CH4) swelled in phosphate-buffered saline (PBS) to reach equilibrium during light irradiation and the temperature was recorded at 1 min intervals for a total of 10 min using a thermal imager (FLIR, E40, with an accuracy of 0.1 °C).

## 2.5 Detection of reactive oxygen species (ROS)

A ROS-sensitive probe, dichlorofluorescein diacetate (DCFH-DA), which is an oxidation-sensitive fluorescent dye, was used to detect ROS generation from the hydrogels under 808 nm NIR light irradiation according to a procedure reported previously. In brief, the samples (CH1, CH2, CH3, and CH4) immersed in the above fluorescent dye solution were exposed to light irradiation and examined at 2 min intervals for 10 min at a power density of 2 W cm<sup>-2</sup>. The fluorescence change in the solution was measured during excitation by 488 nm irradiation and the emission was detected at 525 nm.

## 2.6 Release of copper ions *in vitro*

To obtain the release trend of Cu ions from the hydrogels, the samples were immersed in PBS (pH = 7.4) at 37 °C (>LCST) and 28 °C (<LCST), respectively. The dried samples ( $\varphi$  6 mm × 2 mm) were immersed in 30 mL of PBS. At time intervals of 0.5, 1, 2, 3, 5, 7, and 14 days, 2 mL of the solution were replaced with fresh PBS and the amount of released Cu ions was determined by ICP-AES. In order to determine the influence of the NIR light on the release of Cu ions, the samples were monitored under different conditions (with 808 nm NIR light, or without light irradiation). At time intervals of 10, 20, 30, 50, and 60 min, the amount of released Cu ions was determined by ICP-AES.

## 2.7 *In vitro* antibacterial effects

Two bacteria, *E. coli* and *S. aureus*, were used to evaluate the antibacterial activity of the hydrogels by the spread plate

method. The experimental devices and samples were sterilized with an ultraviolet lamp for at least 30 min and 200  $\mu\text{L}$  of the diluted bacterial suspension ( $10^7$  CFU  $\text{mL}^{-1}$ ) cultured in the sterile Luria-Bertani (LB) medium (containing 1 g of Bactotryptone, 0.5 g of Bacto-yeast extract and 1 g of NaCl in 100 mL of deionized water) were added to 96-well plates containing different types of hydrogels (CH1, CH2, CH3, and CH4), respectively. Each sample was divided into three groups (irradiated for 10 min with 808 nm light or cultured for 10 min or 24 h without light irradiation). For the group with 808 nm light irradiation, the surface temperature was detected by using the thermal imager. Afterwards, 20  $\mu\text{L}$  of the bacterial liquid were taken from the plate and diluted 100 times with the LB medium. After mixing, 20  $\mu\text{L}$  of the diluted bacterial solution were put on a culture dish covered with LB agar and incubated at 37  $^{\circ}\text{C}$  for 24 h. Meanwhile, in order to determine whether the amount of ROS produced under the conditions is actually sufficient to kill the bacteria, the antibacterial experiments were done in an ice bath, eliminating the effect of the temperature. The bacterial colony on the plates was photographed and by counting the number of colonies on the plate, the antibacterial rate was calculated according to eqn (1) ( $N$  is the number of colonies).

$$\text{Antibacterial ratio (\%)} = \frac{N \text{ in control group} - N \text{ in experimental group}}{N \text{ in control group}} \times 100\% \quad (1)$$

## 2.8 Morphological studies

SEM was used to observe the morphology of the bacteria after the antibacterial assay. The samples were taken from the 96-well plates after the last step of antibacterial assay and washed three times with PBS (pH = 7.4) to remove nonadherent bacteria. The bacteria were fixed with 200  $\mu\text{L}$  of 2.5% glutaraldehyde solution for 4 h and dehydrated in alcohol with different concentrations (30, 50, 70, 90, and 100%) for 15 min sequentially. After drying, the bacterial morphology was examined by SEM. In order to examine the change in the inner structure of the bacteria in the long-term treatment, TEM was used. The samples and bacteria were processed by the same way according to the antibacterial procedures. After culturing at 37  $^{\circ}\text{C}$  for 24 h in complete darkness, the bacterial suspensions were centrifuged at 6000 rpm for 5 min. The bacteria were then fixed with 2.5% glutaraldehyde for 2 h and then with 1% aqueous osmium tetroxide at room temperature for 2 h. The samples were washed three times with PBS and dehydrated separately in alcohol with different concentrations (30, 50, 70, 80, 90, and 100%) for 15 min sequentially. Finally, the bacteria were embedded into an embedding medium (acetone:Epon 812 (SPI 90529-77-4) = 1:1) and a sheet of 60 nm made with a diamond knife (Tecnai G220 TWIN) was stained with uranylacetate. The thin section containing the bacteria was placed on a nickel grid for TEM observation.

## 2.9 In vitro cytotoxicity studies

The *in vitro* cytotoxicity of the hydrogels was determined by the 3-[4,5-dimethylthiazol-2-yl]-2,5-diphenyl tetrazolium bromide (MTT) assay using NIH-3T3 cells (mouse embryonic fibroblast cell line). Before the assay, all experimental devices and samples were sterilized with an ultraviolet lamp for at least 30 min. The cells were seeded onto the hydrogels on 96-well plates with 200  $\mu\text{L}$  of the medium and cultured for 1, 3, and 7 days followed by incubation under a humidified atmosphere of 5%  $\text{CO}_2$  at 37  $^{\circ}\text{C}$ . 200  $\mu\text{L}$  of the MTT solution with a concentration of 0.5  $\text{mg mL}^{-1}$  were added to each well after removing the stock solution and incubated at 37  $^{\circ}\text{C}$  for 4 h. After sucking out the solution, 200  $\mu\text{L}$  of the dimethyl sulfoxide (DMSO) solution were added to each well and agitated for 15 min. The supernatant fluid was taken to determine the optical density (OD) on a microplate reader at 490 nm or 570 nm. Meanwhile, in order to explore the safety of the samples in the presence of NIR light, the cells were seeded onto the hydrogels, followed by 10 min irradiation with NIR light or no light irradiation, respectively. After culturing for 1 day, the *in vitro* cytotoxicity of the hydrogels was determined by the MTT assay. The measurements were carried out in triplicate and eqn (2) was used to calculate the inhibition of cell growth.

$$\text{Cell viability (\%)} = \frac{\text{OD in experimental group}}{\text{OD in control group}} \times 100\% \quad (2)$$

## 2.10 Quantitative real-time polymerase chain reaction (Q-RT-PCR)

To study the effects of the CuS NP-based system on the angiogenic-related gene expression of vascular endothelial growth factor (VEGF), basic fibroblast growth factor (bFGF), hypoxia-inducible factor (HIF-1 $\alpha$ ), and glyceraldehyde 3-phosphate dehydrogenase (GAPDH) of the fibroblasts, the Q-RT-PCR technology was implemented. The cells were seeded on 12-well plates and cultured with different hydrogels (CH1, CH2, CH3, and CH4) for 4 and 8 days, respectively. Afterwards, the total RNA was extracted with a Total RNA KIT I (50) (OMEGA R6834-01) and reverse transcribed into cDNA using PrimeScript<sup>TM</sup>RT Master Mix (Perfect Real Time) (Takara) according to the manufacturer's instructions. The resulting cDNA was used as a template for Q-RT-PCR with the target primer for VEGF, bFGF, HIF-1 $\alpha$ , and GAPDH. The relative expression of the genes was normalized against the housekeeping gene GAPDH and the CFX Connect<sup>TM</sup> Real-Time PCR Detection System (Bio-Rad) was used to conduct real-time fluorescence quantification. All the samples were assayed in triplicate and independent experiments. The primer sequences are summarized in Table S1 (ESI<sup>†</sup>).

## 2.11 In vivo animal experiments

Male Wistar rats (180–200 g body weight) obtained from the Hubei Provincial Center for Disease Prevention & Control were used in the animal experiments, and all the animal experi-

ments and procedures were approved by the Hubei Provincial Center for Disease Prevention & Control. All animals were maintained and used in accordance with the Animal Management Rules of the Ministry of Health of the People's Republic of China and the Guidelines for the Care and Use of Laboratory Animals of China. Skin wounds were created on the dorsal area of rats and treated with different samples. The rats were individually raised in cages at a standard temperature for 2 days and randomly divided into three groups with four rats in each group: 3 M wound dressing (group I, conventional wound therapy, Minnesota Mining and Manufacturing Medical Equipment (Shanghai) Co., Ltd), pure hydrogel (CH1, group II), NPs-Hydrogel (CH4, group III). After anesthesia with 10% chloral hydrate ( $30 \text{ mg kg}^{-1}$ ), the dorsal area of the rat was totally depilated and one full-thickness circular wound (about 6 mm in diameter) was created on the upper back of each rat. After adding 20  $\mu\text{L}$  of the diluted bacterial suspension ( $10^8 \text{ CFU mL}^{-1}$ ) to the wounds and absorption for about 5 min, the wounds of the three groups were treated with the standard 3 M wound dressing, CH1 and CH4, respectively. After irradiation with 808 nm light for 10 min, the wounds of the three groups were tightly wrapped by nonopaque sterile medical tapes and the rats were individually raised in cages at a standard temperature. Each dressing was changed every 2 days and the process continued for 14 days. After 2, 4, 8, and 14 days, the wounds were examined and photographed. The rats were sacrificed on day 14 and the wound site with the surrounding skin was harvested and fixed with 10% formalin. The central wound sections were fixed on glass slides and stained with Giemsa staining on day 2 and hematoxylin and eosin (H&E) on days 2, 4, 8, and 14. Giemsa and H&E staining were used to evaluate the amount of adherent bacteria around the wounds and wound-healing progress, respectively.

### 3. Results and discussion

#### 3.1 Characterization of the nanocomposite hydrogels

As shown in Fig. S1a,† the average size of the CuS NPs is about 10 nm with a multi-crystalline structure. To graft the CuS NPs onto the hydrogel tightly and uniformly, the NPs are functionalized. Fig. S1b† shows that the microspheres with a total diameter of about 25 nm are coated with a layer of  $\text{mSiO}_2$  to form a well-dispersed solution. The full XPS spectra (Fig. S2a†) suggest the presence of Cu, S, C, O, N and Si. As shown in Fig. S2b,† the C 1s peaks obtained from the CuS/ $\text{mSiO}_2$  NPs can be deconvoluted into four subpeaks at 288.8, 286.5, 285.4, and 284.8 eV corresponding to  $\text{O}=\text{C}-\text{OH}$ , C–O, C–N, and C–C, respectively. The peaks of C and O suggest carboxyl surface functionalization and the Si and N peaks arise from silicon dioxide and amino on the hybrid NPs, respectively. The Cu 2p peaks, namely Cu  $2\text{p}_{3/2}$  and Cu  $2\text{p}_{1/2}$ , appear at 932.12 and 952.08 eV (Fig. S2c†) corresponding to Cu(II). The S 2p peak at 162.18 eV (Fig. S2d†) indicates the presence of S in the CuS NPs.<sup>43</sup> Fig. S3† shows that the IR peaks around 3422 and 1617  $\text{cm}^{-1}$  correspond to the functional groups of O–H and

C=O of carboxyl. Because of the conjugation effects, the absorption peak of C=O in carboxyl shifts to a smaller wavenumber. After functionalization by  $\text{mSiO}_2$ , the characteristic IR peak at 1083  $\text{cm}^{-1}$  is strong and broad corresponding to the asymmetrical stretching vibration absorption of Si–O. After grafting the MPS functional group, the IR peaks of the hybrid NPs at 1718 and 1601  $\text{cm}^{-1}$  are the characteristic IR peaks of MPS due to C=O and C=C, respectively. It can be concluded that the CuS NPs are grafted with carbon–carbon double bonds *via* MPS modification.

After radical polymerization, the functional hybrid NPs, CuS/ $\text{mSiO}_2$ -MPS, are embedded in a poly(NIAAm-*co*-AAM) hydrogel. The pure hydrogel has a macroporous sponge-like structure and most of the pores resemble a rectangle (Fig. S4†). After the incorporation of functional CuS NPs, the porous structure of the NPs-Hydrogel is maintained but the pores are smaller and have a circular shape (Fig. 1b). The images of the sol and gel states prepared from the polymer aqueous solution are shown in Fig. 1c. After polymerization for 4 h, the solution is completely converted into gel. The reason for the difference in the morphology is probably that the radical polymerization can be catalyzed by copper ions<sup>44</sup> and thus the cross-linking degree in the NPs-Hydrogel may be higher than that of the pure hydrogel. The uniform distribution of NPs in the hydrogel is confirmed by EDS elemental mapping as shown in Fig. 1d and e. According to the calculation of peak areas, the molar ratio of Cu/S is  $\sim 0.1:0.15$ , which is very close to the one in CuS (Fig. S5†). As shown in Fig. S6a,† the characteristic IR peaks around 2972 and 2929  $\text{cm}^{-1}$  are assigned to the  $\text{CH}_3$  and  $\text{CH}_2$  stretching vibrations, respectively and those at 1644 and 1543  $\text{cm}^{-1}$  are attributed to the secondary amide of C=O stretching and N–H bending vibrations in the copolymer, respectively. The IR peaks only appear from the NPs-Hydrogel at around 1749 and 1097  $\text{cm}^{-1}$  and are assigned to ester carbonyl and Si–O stretching vibration, respectively. The NPs-Hydrogel shows diffraction peaks from the (102), (103), (006), (110) and (116) planes matching the pure hexagonal CuS structure (JCPDS card no. 06-0464),<sup>43,45</sup> further proving successful loading of CuS NPs into the hydrogel (Fig. S6b†). By comparing the spectra, the occurrence of a wide peak at  $\sim 23^\circ$  stems from the polymer substrate.

As shown in Fig. S6c,† the CuS NPs exhibit enhanced absorption in the NIR region due to localized surface plasmon resonance (LSPR), based on their intrinsic copper vacancies in the lattice.<sup>46–48</sup> The NPs-Hydrogel exhibits a similar spectrum to that of CuS NPs but the pure hydrogel shows no absorption in this wavelength region. Strong absorption by the hydrogels in the NIR region enables potential application in PTT and PDT under NIR laser irradiation. The water contact angle (WCA) on the pure hydrogel changes little with NIR irradiation but the NIR irradiated NPs-Hydrogel shows an increasing WCA as the irradiation time increases (Fig. S6d†). After NIR exposure for 10 min, the WCA of the NPs-Hydrogel is about  $100^\circ$ , much higher than  $40.5^\circ$ , the WCA of the unexposed hydrogel. It has been demonstrated that poly-NIAAm and its

derivatives can swell and shrink significantly in an aqueous environment at temperatures below and above the LCST, respectively. This transition is mainly controlled by the rapid alteration in the hydrophilicity and hydrophobicity among the hydrogel sub-groups and structural collapse takes place upon heating.<sup>42</sup> Volume shrinkage caused by heating is resulting the burst release of soluble materials and the change from hydrophilic to hydrophobic on the hydrogels.<sup>49,50</sup> The change in the WCA shows that the NPs-Hydrogel absorbs energy from photons and dissipates it partially in the form of heat ascribed to absorption in the NIR region.

### 3.2 *In vitro* photothermal effects and reactive oxygen species (ROS) detection

As shown in Fig. 2a, during NIR light irradiation, the surface temperatures of all the NP-samples increase rapidly and reach a plateau after irradiation for 8 min. Upon NIR laser irradiation, the d-d energy band transition of Cu(II) ions can be triggered, leading to the photothermal performance.<sup>46</sup> The maximal temperature of CH1, CH2, CH3 and CH4 is 29.1 °C, 43.7 °C, 52.1 °C, and 59.5 °C, respectively. Obviously, more CuS NPs in the hybrid hydrogels lead to a higher temperature during NIR irradiation due to more absorption of NIR by the CuS NPs, indicating the concentration-dependent features. The laser on-off cycles of CH4 in Fig. 2b disclose that repeated irradiation does not significantly influence the photothermal properties. The produced hyperthermia shown in Fig. 2c illustrates that after embedding with CuS NPs, NIR light can be

absorbed and then converted into heat *via* the photothermal effects of CuS NPs in the hydrogels.

ROS generation is determined by the fluorescence signal of a ROS sensitive probe, DCFH-DA. DCFH-DA is nonfluorescent but can be rapidly oxidized to a highly fluorescent molecule (dichlorofluorescein, DCF) in the presence of ROS.<sup>51</sup> So the production of ROS induced by the NIR light irradiated samples can be inferred from the increased fluorescence absorbance at 525 nm. As shown in Fig. 2d, the fluorescence intensity (FI) increases with more embedded NPs and longer illumination time at the same power intensity ( $2 \text{ W cm}^{-2}$ ). After light irradiation of the CH4 sample for 10 min, an 8.1 fold enhancement in the FI of DCF is detected at 525 nm compared to sample CH4 without NIR light irradiation (Fig. 2e). As for CH1, the change in FI is negligible with or without light irradiation (Fig. S7a†). CuS nanomaterials are p-type semiconductors with a high density of free carriers (hole carriers) and strong LSPR.<sup>52,53</sup> Under NIR light irradiation, a large amount of hole carriers in CuS NPs may produce more hydroxyl radicals ( $\cdot\text{OH}$ ) through a reaction between holes and water molecules. The generation of ROS is also detected from the light-irradiated CH2 (Fig. S7b†) and CH3 (Fig. S7c†). Fig. S7d† shows similar FI in the DCFH-DA dye at different temperatures (25 °C, 50 °C, and 60 °C), indicating that the dye is very stable between 25 and 60 °C. The results suggest that the ROS generation in hydrogels induced by 808 nm light irradiation is concentration and irradiation time dependent. The illustration of the photothermal and photodynamic per-

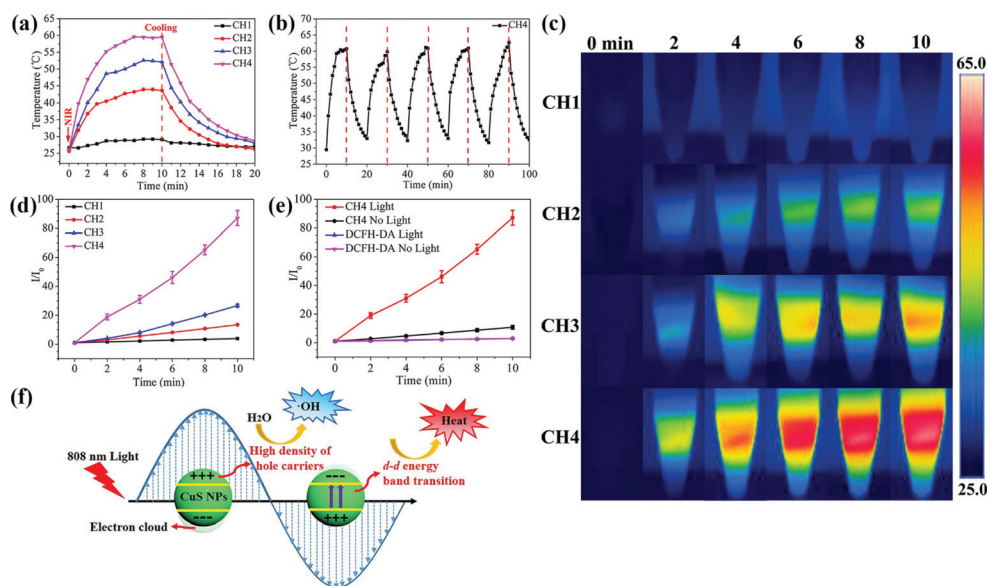


**Fig. 2** (a) Heating/cooling experiments of the hydrogels in the PBS aqueous solution under 808 nm laser irradiation at a power density of  $2 \text{ W cm}^{-2}$ . (b) Transient thermal measurements of the hydrogel under repeated laser on-off cycles of NIR light irradiation ( $2 \text{ W cm}^{-2}$ ). Five cycles of 808 nm light irradiation are carried out on CH4 and each cycle consists of 10 min irradiation followed by a 10 min cooling phase. (c) Real-time infrared thermal images of different hydrogels immersed into PBS aqueous solution under  $2 \text{ W cm}^{-2}$  continuous NIR light irradiation for 10 min. (d) Fluorescence intensity (FI) of DCF at 525 nm with different hydrogels immersed in the fluorescent dye solution and irradiated with NIR light at a power density of  $2 \text{ W cm}^{-2}$ .  $I_0$ : FI in initial value,  $I$ : FI at different times. (e) FI of DCF at 525 nm in CH4 and DCFH-DA dyes under light or no light conditions, respectively. (f) Illustration of photothermal and photodynamic performance process in hydrogel under NIR light. The experiments are performed in triplicate and independently.

formance process of the CuS-based biomaterials under NIR light is shown in Fig. 2f.

### 3.3 Detection of released copper ions

Fig. 3a exhibits the cumulative concentration of Cu ions released from the different hydrogels (CH2, CH3, and CH4) to the PBS (pH = 7.4) at 37 °C. The samples show a similar release behavior with slow release observed in the first 2 days, relatively rapid release in the subsequent 5 days, and stabilization afterwards. CH4 shows the biggest release and CH2 is the smallest, consistent with the embedded CuS NP contents. The Cu ions are formed by the dissociation of ions from the CuS NPs.<sup>28</sup> For the hydrogel poly(NIAAm-co-AAm) with a molar ratio of 95 : 5, the unique volume transition at LCST in water is around 35 °C (Fig. S8†) and it swells and shrinks significantly in an aqueous environment at temperature below and above the LCST, respectively.<sup>42</sup> At 37 °C (>LCST) in PBS, volume shrinkage is observed from the hydrogel and the volume transition of the hydrogel may impact the release of Cu ions. The sample (CH3) is monitored in PBS (pH = 7.4) at 28 °C (<LCST) and 37 °C (>LCST), respectively. As shown in Fig. S9a,† the amount of Cu ions is nearly equal in the first two days in spite of the different temperatures. However, starting from the third day, the release rate at 37 °C is bigger than that at 28 °C. Fig. S9b† shows the change in the diameters of the samples at different temperatures. The diameter of the swollen hydrogel decreases from 8 mm to 5.1 mm after soaking in PBS at 37 °C for 2 days but the volume remains almost unchanged in the next days. In contrast, the volume remains at about 8 mm all the time at 28 °C. The Cu ions interact with the carrier hydrogel by electrostatic or van der Waals forces. When the volume of the hydrogel shrinks, electrostatic repulsion between ions spurs easier release of ions and so after 2 days, rapid release of copper ions is observed and so there is evidence that shrinkage of the hydrogel increases the release of Cu ions.

To explore the effects of NIR light on the release of Cu ions, one sample (CH3) is monitored with or without light, respectively. As shown in Fig. 3b, the release rates of Cu ions under light illumination are larger. The possible reason is that as the CuS embedded hydrogel absorbs NIR light and converts it into heat, the volume shrinkage results in the burst release of soluble materials in the hydrogel carrier. Hence, the tempera-

ture response as a result of NIR irradiation makes the hydrogel a special carrier in drug delivery systems.

### 3.4 Antibacterial activity *in vitro*

The antibacterial activity of the hydrogels against *S. aureus* and *E. coli* is determined by the spread plate method. In general, the samples exhibit almost the same antibacterial trend against *S. aureus* and *E. coli*. The light irradiated samples (CH2, CH3, and CH4) show enhanced antibacterial efficacy against both *S. aureus* (Fig. 4a) and *E. coli* (Fig. 4b). As the content of CuS in the hydrogel is increased, the antibacterial efficacy of CH2, CH3, and CH4 goes up to 62.38%, 98.03%, and 99.80% against *S. aureus* (Fig. 4c) and 42.14%, 99.68%, and 99.94% against *E. coli* (Fig. 4d), respectively. In contrast, with or without light, the bacterial colonies of the control group (CH1) are the same so that CH1 has no antibacterial activity. Furthermore, without light irradiation, the bacterial counts on the samples change slightly regardless of the CuS content in the hydrogel. The corresponding antibacterial ratios are 0%, 10.82%, and 17.86% against *S. aureus* and 0%, 24.87%, and 27.96% against *E. coli*, respectively. The results suggest that hyperthermia (Fig. 2a) and ROS (Fig. 2d) produced from the CuS NPs by NIR irradiation for a short time are responsible for the antibacterial activity of the hybrid hydrogels. The small antibacterial activity may be ascribed to smaller concentrations of released Cu ions (Fig. 3b) in darkness for 10 min. The morphology and membrane integrity of the bacteria treated with the samples are examined by SEM. Fig. 4e and f show that the *S. aureus* and *E. coli* cells are attached to the hydrogel and with or without light, *S. aureus* and *E. coli* incubated with CH1 show a compact morphology with a smooth surface, demonstrating that the polymer has little toxicity against bacteria. In contrast, the bacteria treated with the hydrogels embedded with CuS NPs (CH2, CH3, and CH4) are influenced by NIR light greatly. The membranes become rough and wrinkled or even cracks are observed after irradiation for 10 min as marked by red arrows for *S. aureus* and blue arrows for *E. coli*. In comparison, without light irradiation, the typical morphology of *S. aureus* and *E. coli* with a smooth surface and spherical and rod shape, respectively, is observed from CH2 and CH3 and only slight damage appears from CH4.

The individual effects of ROS produced by CuS NPs on the antibacterial effect are shown in Fig. S10.† The bacterial counts on the sample CH4 change slightly compared to the control group of CH1, so it shows that the antibacterial effect of individual ROS in this work is not significant. The effects of Cu ions on the antibacterial activity are shown in Fig. 5. After culturing for 24 h in darkness, the bacterial colonies of both *S. aureus* and *E. coli* decrease gradually with increased concentrations of embedded NPs compared to the control group of CH1 (Fig. 5a). CH4 shows countable colonies with antibacterial rates of 88.87% and 95.91% against *S. aureus* and *E. coli* (Fig. 5b and c), respectively. Since no hyperthermia and ROS can be produced in darkness, the higher antibacterial efficacy

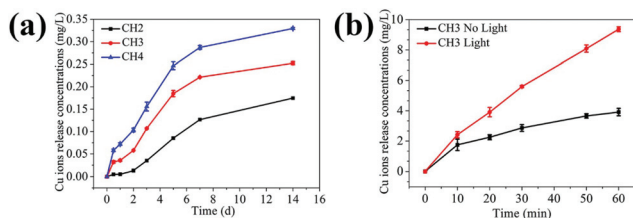


**Fig. 3** (a) Cumulative amounts of Cu ions released from the hydrogels (CH2, CH3, and CH4) after immersion in PBS at 37 °C for 14 days. (b) Cumulative amounts of Cu ions released from CH3 (the amount of samples in experiment (b) is higher than (a)) to PBS with and without light. The experiments are performed in triplicate and independently.

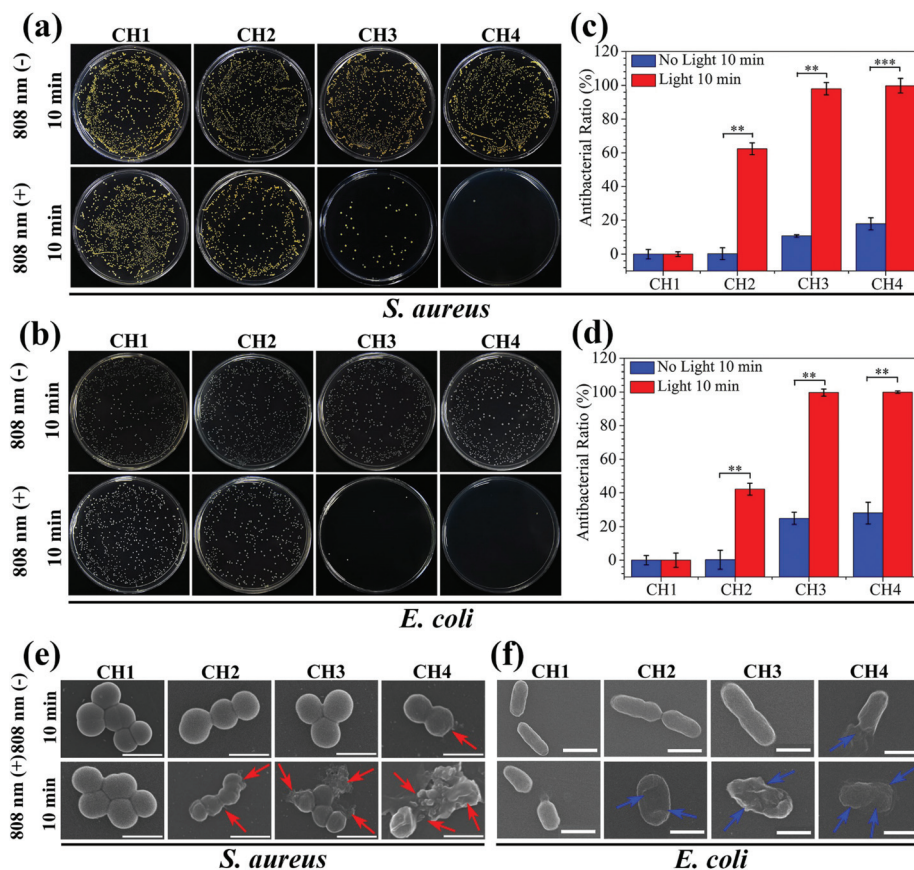


**Fig. 4** *In vitro* antibacterial assay showing the spread plate results of (a) *S. aureus* and (b) *E. coli*. The formed viable colony units after treating the bacteria with hydrogels with and without NIR light illumination for 10 min, diluting the bacterial solution, spreading on LB agar plates, and incubating at 37 °C for 24 h. The histograms of the antibacterial ability of (c) *S. aureus* and (d) *E. coli*. SEM morphology of (e) *S. aureus* (red arrows) and (f) *E. coli* (blue arrows) treated with different hydrogels (CH1, CH2, CH3, and CH4). Scale bars are 1  $\mu\text{m}$  and error bars indicate means  $\pm$  standard deviations: \* $P < 0.05$ , \*\* $P < 0.01$ , and \*\*\* $P < 0.001$ .

observed from CH4 after culturing for 24 h is ascribed to the released Cu ions.<sup>54,55</sup>

To further investigate the antibacterial activity of the samples, the membrane damage and intracellular structural change of *S. aureus* and *E. coli* are observed by TEM and EDS. Fig. 5d shows that the *S. aureus* and *E. coli* cells have the normal morphology with distinct cell walls and compact intracellular substrates when cultured with pure hydrogel (CH1). However, obvious distortion is detected from the bacteria after culturing with NPs-Hydrogel (CH4). EDS shows the existence of the Cu inside of the broken cells (red rectangles) in CH4, indicating the penetration of Cu ions into the bacterial membrane. After culturing for 24 h with the bacteria, the Cu ions also assist in sterilization. Cu ions released from CH4 may be absorbed by the bacteria, then damage the cell membrane, solidify the structure of proteins, or alter the function of enzymes. Cu ions can be cytotoxic and the primary bacteria killing mechanism includes the inactivation of central catabolic and biosynthetic pathways.<sup>55</sup> As shown in Fig. 5d marked by yellow arrows, the intracellular substrates in the broken bacterial cells become disordered and there are a lot of white spaces on the inside of the cells. This may originate from

the damage of proteins or enzymes in the cells caused by Cu ions.

According to our results, the hydrogel embedded with functional CuS NPs exhibits favourable photothermal and photodynamic effects under the 808 nm NIR light irradiation. The heat damages the membrane integrity and cell viability, and ROS-mediated oxidative stress compromises bacterial metabolism and membrane structure eventually causing cell death. In addition, the antibacterial action rendered by the released Cu ions enhances the antibacterial effects synergistically. Although the antibacterial action of Cu ions requires a relatively long time, light irradiation can shorten the time enabling bacterial killing in a short time.

### 3.5 *In vitro* cell response to the nanocomposite hydrogels

To be viable clinically, the biomaterials should possess both antimicrobial ability and biocompatibility and therefore, the cytotoxicity is investigated by the MTT assays. As shown in Fig. 6a, after culturing for 3 days, the hydrogels (CH2, CH3, and CH4) show larger inhibition ratios against NIH-3T3 cells with increasing concentration of embedded NPs. In the experiments, the culture medium is refreshed in three days and the



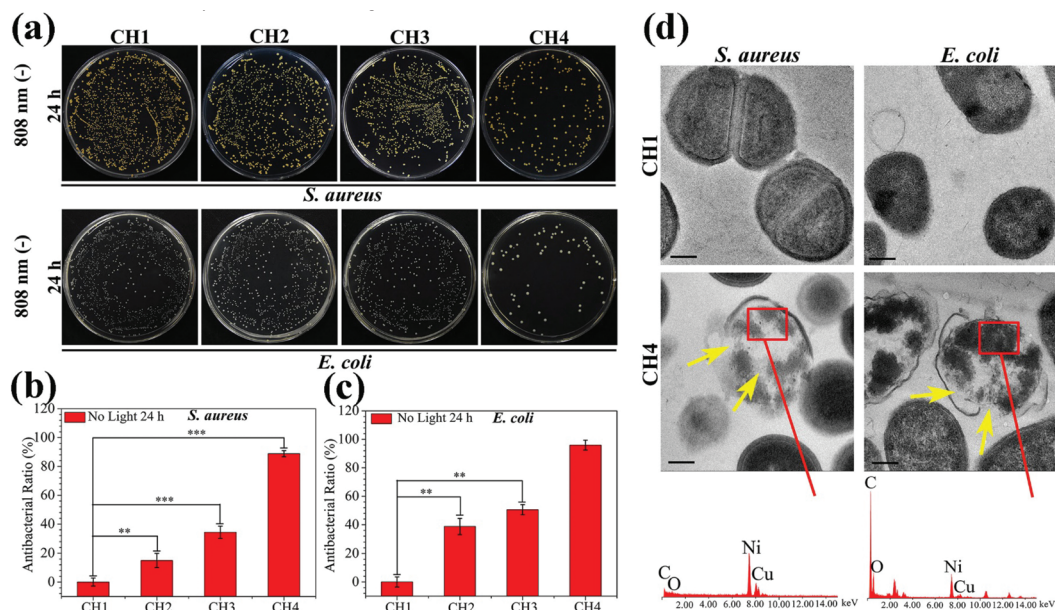


**Fig. 5** *In vitro* antibacterial assay with no light irradiation and culturing for 24 h in darkness. (a) Spread plate results of *S. aureus* and *E. coli*. Histogram of the antibacterial ability of (b) *S. aureus* and (c) *E. coli*. (d) TEM images and the corresponding EDS analysis of the bacterial intracellular sections of CH1 and CH4 respectively. Scale bars are 200 nm and the error bars indicate means  $\pm$  standard deviations: \* $P < 0.05$ , \*\* $P < 0.01$ , and \*\*\* $P < 0.001$ .

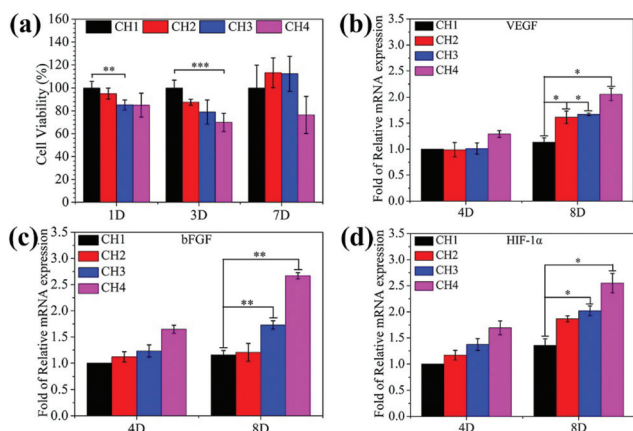


**Fig. 6** (a) Cell viability of NIH-3T3 treated with hydrogels CH1, CH2, CH3, and CH4 at day 1, 3, and 7. Gene expression measured by Q-RT-PCR of the angiogenic genes; (b) VEGF, (c) bFGF, and (d) HIF-1 $\alpha$  for fibroblasts incubated for 4 and 8 days in media containing different hydrogels (CH1, CH2, CH3, and CH4). The error bars indicate means  $\pm$  standard deviations: \* $P < 0.05$ , \*\* $P < 0.01$ , and \*\*\* $P < 0.001$ .

cell viability improves to more than 100% for CH2 and CH3 and 76.39% for CH4 after 7 days. Cu ions directly or indirectly stimulate many factors important for the proliferation of fibroblasts.<sup>31,33,56</sup> The growth factor may facilitate the proliferation of cells in CH2 and CH3 at day 7 and in comparison, slightly higher inhibition is observed from CH4 because of excessive Cu ions as shown in Fig. 3a. As shown in Fig. S11,<sup>†</sup> after NIR light irradiation, the hydrogels (CH2, CH3, and CH4) show larger inhibition ratios against NIH-3T3 cells, because of

hyperthermia (Fig. 2a) and ROS (Fig. 2d) produced from the CuS NPs by NIR irradiation. But there are still enough cells to survive, and the corresponding cell viability is 77.49% for CH2, 61.11% for CH3, and 37.08% for CH4. It shows that short periods of light can affect the cell growth, but not completely. The results reveal that the hydrogels with smaller concentrations of NPs do not exhibit appreciable negative effects on the cell viability demonstrating the good biocompatibility.

The gene expression of VEGF (Fig. 6b), bFGF (Fig. 6c), and HIF-1 $\alpha$  (Fig. 6d) for fibroblasts incubated in the medium containing different hydrogels increases with increasing concentration of embedded CuS NPs at incubation time points of 4 and 8 days. As expected, after 8 days, NPs-Hydrogels show a higher mRNA level of VEGF, bFGF, and HIF-1 $\alpha$  than the control (CH1). As an important factor in angiogenesis, the gene expression of VEGF and bFGF is related to the angiogenic response and HIF-1 $\alpha$  mimicking hypoxia plays a critical role in the recruitment and differentiation of cells and in blood vessel formation.<sup>33</sup> Stimulation of the gene expression suggests that the hybrid hydrogels have strong stimulatory effects on upregulation of the angiogenic growth factors.

### 3.6 *In vivo* animal experiments

Fig. 7a shows wound closure at different time points. The wound treated with CH4 in group III heals after treatment for 2 weeks but those of other groups still show clear defects. The change in the wound area in Fig. 7b reveals that the wounds in group III have a smaller trauma size than those in other groups at all time. During the experiments, all the groups show severe bacterial infection after the 2 day treatment. The

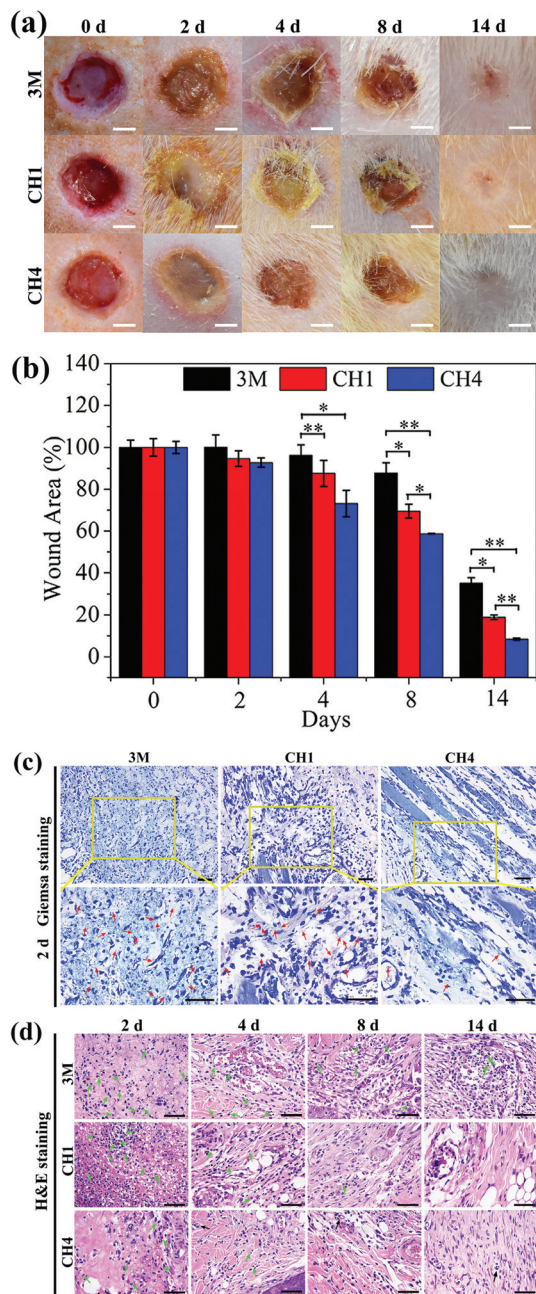


**Fig. 7** *In vivo* assessment of the hydrogels with antibacterial effects and wound healing capability (group I: 3 M wound dressing; group II: CH1, pure hydrogel; group III: CH4, hydrogel embedded with CuS NPs in  $1.5 \text{ mg mL}^{-1}$ ). (a) Photographs of the *S. aureus*-infected wound treated with different dressings at time points of 0, 2, 4, 8, and 14 days. Scale bars, 2 mm. (b) Corresponding wound area at the different time points. (c) Giemsa stained images showing the degree of infection in the wound area after a 2 day treatment. Scale bars are  $50 \mu\text{m}$ . (d) H&E stained images showing the degree of infection of the skin tissue after 2, 4, 8, and 14 days. Scale bars are  $50 \mu\text{m}$ . The error bars indicate means  $\pm$  standard deviations: \* $P < 0.05$ , \*\* $P < 0.01$ , and \*\*\* $P < 0.001$ .

amount of adherent bacteria around the wound is observed by Giemsa staining (red arrows) as shown in Fig. 7c. By counting the amount of bacteria stained by Giemsa, the quantitative

analysis of *in vivo* antibacterial effects is presented in Fig. S12.† Compared to groups I and II, the amount of bacteria in group III decreases significantly due to the antibacterial ability of CH4 *in vivo*. The number of neutrophils in soft tissues also indicate bacterial infection because neutrophils migrate rapidly from circulating blood to infected sites in response to infection.<sup>57</sup> As shown in Fig. 7d, many lobulated neutrophils can be observed surrounding the wounds marked by the green arrows after H&E staining, thereby indicating severe bacterial infection especially in groups I and II in the first 4 days. In comparison, the number of neutrophils in group III is less and the majority of the cells are normal indicative of relatively minor infection and effective antibacterial ability of CH4 *in vivo*. In particular, after the 4 day treatment, new blood vessels (black arrow) are observed from group III aided by Cu ions released from NPs-Hydrogel.<sup>31–33</sup> Comparing groups I and II, recovery in group II is better and so a moist wound environment indeed facilitates wound healing.<sup>36–38</sup>

The *in vivo* microscopic therapeutic efficacy is assayed by blood routine analysis as shown in Fig. S13.† The parameters, white blood cells (WBCs) (Fig. S13a†) and neutrophils (Fig. S13b†), tested in the treated groups are within the normal ranges. Furthermore, as shown in Fig. S13c,† the histological analysis of the major organs (heart, liver, spleen, lung, and kidney) does not indicate any abnormal effects or damage after the 14-day treatment, suggesting that the NPs-Hydrogels are safe *in vivo*.

## 4. Conclusions

A stimulus-responsive hydrogel system embedded with functional inorganic CuS NPs is designed and fabricated. The biomaterials possess an antibacterial efficacy of 99.80% and 99.94% against *S. aureus* and *E. coli* within 10 min after application, respectively, due to the combined action of PTT, PDT and copper ions under NIR light irradiation. The volume variation in this hybrid hydrogel can be controlled by the NIR light to alter the rate of release of copper ions to the physiological environment. Cu ions released from the hydrogels stimulate the proliferation and angiogenesis of cells to accelerate wound healing. The NPs-Hydrogel is demonstrated to have the ability to kill bacteria while promoting healing of wounds. The excellent performance stems from the combined effects of hyperthermia, radical oxygen species, and released copper ions produced during NIR irradiation of NPs-Hydrogels.

## Conflicts of interest

There are no conflicts to declare.

## Acknowledgements

This work is jointly supported by the National Natural Science Foundation of China, 51671081, and 51422102, the National

Key Research and Development Program of China, no. 2016YFC1100600 (subproject 2016YFC1100604), the Hong Kong Research Grants Council (RGC) General Research Funds (RGC) General Research Funds (GRF) no. CityU 11301215, and 11205617, Hong Kong ITC (ITS/287/17, GHX/002/14SZ), the Health and Medical Research Fund (03142446), as well as Hong Kong RGC GRF (17214516) and RGC/NSFC (N\_HKU725-16) and the Natural Science Fund of Hubei Province, 2018CFA064.

## References

- 1 M. Urdea, L. A. Penny, S. S. Olmsted, M. Y. Giovanni, P. Kaspar, A. Shepherd, P. Wilson, C. A. Dahl, S. Buchsbaum, G. Moeller and D. C. Hay Burgess, *Nature*, 2006, **444**, 73–79.
- 2 N. K. Tittikpina, F. Nana, S. Fontanay, S. Philippot, K. Batawila, K. Akpagana, G. Kirsch, P. Chaimbault, C. Jacob and R. E. Duval, *J. Ethnopharmacol.*, 2018, **212**, 200–207.
- 3 L. j. Zhang, C. F. Guerrero-Juarez, T. Hata, S. P. Bapat, R. Ramos, M. V. Plikus and R. L. Gallo, *Science*, 2015, **347**, 67–71.
- 4 R. M. Klevens, M. A. Morrison, J. Nadle, S. Petit, K. Gershman, S. Ray, L. H. Harrison, R. Lynfield, G. Dumyati, J. M. Townes, A. S. Craig, E. R. Zell, G. E. Fosheim, L. K. McDougal, R. B. Carey and S. K. Fridkin, *JAMA*, 2007, **298**, 1763–1771.
- 5 K. A. Engebretsen and J. P. Thyssen, *Curr. Probl. Dermatol.*, 2016, **49**, 90–102.
- 6 D. J. Tobin, *Chem. Soc. Rev.*, 2006, **35**, 52–67.
- 7 S. H. MacVane, *J. Intensive Care Med.*, 2016, **32**, 25–37.
- 8 X. Xie, C. Mao, X. Liu, Y. Zhang, Z. Cui, X. Yang, K. W. K. Yeung, H. Pan, P. K. Chu and S. Wu, *ACS Appl. Mater. Interfaces*, 2017, **9**, 26417–26428.
- 9 A. Panáček, L. Kvítek, M. Smékalová, R. Večeřová, M. Kolář, M. Röderová, F. Dyčka, M. Šebela, R. Prucek, O. Tomanec and R. Zbořil, *Nat. Nanotechnol.*, 2018, **13**, 65–71.
- 10 C. Mao, Y. Xiang, X. Liu, Z. Cui, X. Yang, K. W. K. Yeung, H. Pan, X. Wang, P. K. Chu and S. Wu, *ACS Nano*, 2017, **11**, 9010–9021.
- 11 X. Zhang, L. Y. Xia, X. Chen, Z. Chen and F. G. Wu, *Sci. China Mater.*, 2017, **60**, 487–503.
- 12 J. Huang, J. Zhou, J. Zhuang, H. Gao, D. Huang, L. Wang, W. Wu, Q. Li, D. P. Yang and M. Y. Han, *ACS Appl. Mater. Interfaces*, 2017, **9**, 36606–36614.
- 13 L. Tan, J. Li, X. Liu, Z. Cui, X. Yang, K. W. K. Yeung, H. Pan, Y. Zheng, X. Wang and S. Wu, *Small*, 2018, **14**, 1703197.
- 14 A. L. Chin, Y. Zhong and R. Tong, *Biomater. Sci.*, 2017, **5**, 1491–1499.
- 15 Y. Z. Chen, W. H. Li, L. Li and L. N. Wang, *Rare Met.*, 2018, **37**, 1–12.
- 16 B. Liu, C. Li, Z. Cheng, Z. Hou, S. Huang and J. Lin, *Biomater. Sci.*, 2016, **4**, 890–909.
- 17 H. Zhu, P. Cheng, P. Chen and K. Pu, *Biomater. Sci.*, 2018, **6**, 746–765.
- 18 H. J. Yoon, H. S. Lee, J. Y. Lim and J. H. Park, *ACS Appl. Mater. Interfaces*, 2017, **9**, 5683–5691.
- 19 B. Zhang, H. Wang, S. Shen, X. She, W. Shi, J. Chen, Q. Zhang, Y. Hu, Z. Pang and X. Jiang, *Biomaterials*, 2016, **79**, 46–55.
- 20 X. Guo, W. Li, J. Zhou, W. Hou, X. Wen, H. Zhang, F. Kong, L. Luo, Q. Li, Y. Du and J. You, *Small*, 2017, **13**, 1603270.
- 21 H. Jiang, D. Chen, D. Guo, N. Wang, Y. Su, X. Jin, G. Tong and X. Zhu, *Biomater. Sci.*, 2017, **5**, 686–697.
- 22 M. S. Yavuz, Y. Cheng, J. Chen, C. M. Cobley, Q. Zhang, M. Rycenga, J. Xie, C. Kim, K. H. Song, A. G. Schwartz, L. V. Wang and Y. Xia, *Nat. Mater.*, 2009, **8**, 935–939.
- 23 H. Liu, T. Liu, L. Li, N. Hao, L. Tan, X. Meng, J. Ren, D. Chen and F. Tang, *Nanoscale*, 2012, **4**, 3523–3529.
- 24 Q. Tian, F. Jiang, R. Zou, Q. Liu, Z. Chen, M. Zhu, S. Yang, J. Wang, J. Wang and J. Hu, *ACS Nano*, 2011, **5**, 9761–9771.
- 25 Q. You, Q. Sun, J. Wang, X. Tan, X. Pang, L. Liu, M. Yu, F. Tan and N. Li, *Nanoscale*, 2017, **9**, 3784–3796.
- 26 R. Lv, P. Yang, B. Hu, J. Xu, W. Shang and J. Tian, *ACS Nano*, 2016, **11**, 1064–1072.
- 27 W. Yang, W. Guo, W. Le, G. Lv, F. Zhang, L. Shi, X. Wang, J. Wang, S. Wang, J. Chang and B. Zhang, *ACS Nano*, 2016, **10**, 10245–10257.
- 28 L. Guo, I. Panderi, D. D. Yan, K. Szulak, Y. Li, Y. T. Chen, H. Ma, D. B. Niesen, N. Seeram, A. Ahmed, B. Yan, D. Pantazatos and W. Lu, *ACS Nano*, 2013, **7**, 8780–8793.
- 29 S. Wang, A. Riedinger, H. Li, C. Fu, H. Liu, L. Li, T. Liu, L. Tan, M. J. Barthel, G. Pugliese, F. D. Donato, M. S. D'Abbusco, X. Meng, L. Manna, H. Meng and T. Pellegrino, *ACS Nano*, 2015, **9**, 1788–1800.
- 30 L. Hou, X. Shan, L. Hao, Q. Feng and Z. Zhang, *Acta Biomater.*, 2017, **54**, 307–320.
- 31 N. Kong, K. Lin, H. Li and J. Chang, *J. Mater. Chem. B*, 2014, **2**, 1100–1110.
- 32 X. Wang, F. Lv, T. Li, Y. Han, Z. Yi, M. Liu, J. Chang and C. Wu, *ACS Nano*, 2017, **11**, 11337–11349.
- 33 S. Zhao, L. Li, H. Wang, Y. Zhang, X. Cheng, N. Zhou, M. N. Rahaman, Z. Liu, W. Huang and C. Zhang, *Biomaterials*, 2015, **53**, 379–391.
- 34 B. Cao, Y. Zheng, T. Xi, C. Zhang, W. Song, K. Burugapalli, H. Yang and Y. Ma, *Biomed. Microdevices*, 2012, **14**, 709–720.
- 35 K. L. S. Worthington, A. Adamcakova-Dodd, A. Wongrakpanich, I. A. Mudunkotuwa, K. A. Mapuskar, V. B. Joshi, C. A. Guymon, D. R. Spitz, V. H. Grassian, P. S. Thorne and A. K. Salem, *Nanotechnology*, 2013, **24**, 395101.
- 36 G. D. Winter, *Nature*, 1962, **193**, 293–294.
- 37 C. K. Field and M. D. Kerstein, *Am. J. Surg.*, 1994, **167**, S2–S6.
- 38 H. C. Korting, C. Schöllmann and R. J. White, *JEADV*, 2011, **25**, 130–137.
- 39 Y. Li, Y. Han, X. Wang, J. Peng, Y. Xu and J. Chang, *ACS Appl. Mater. Interfaces*, 2017, **9**, 16054–16062.
- 40 D. Seliktar, *Science*, 2012, **336**, 1124–1128.
- 41 A. S. Hoffman, *Adv. Drug Delivery Rev.*, 2012, **64**, 18–23.

- 42 X. Z. Zhang, D. Q. Wu and C. C. Chu, *Biomaterials*, 2004, **25**, 3793–3805.
- 43 V. V. Kumar, P. S. Hariharan, D. Eniyavan, N. Hari and S. P. Anthony, *CrystEngComm*, 2015, **17**, 3452–3459.
- 44 J. S. Wang and K. Matyjaszewski, *Macromolecules*, 1995, **28**, 7901–7910.
- 45 Y. Xie, G. Bertoni, A. Riedinger, A. Sathya, M. Praro, S. Marras, R. Tu, T. Pellegrino and L. Manna, *Chem. Mater.*, 2015, **27**, 7531–7537.
- 46 Y. Chang, Y. Cheng, Y. Feng, H. Jian, L. Wang, X. Ma, X. Li and H. Zhang, *Nano Lett.*, 2018, **18**, 886–897.
- 47 A. Comin and L. Manna, *Chem. Soc. Rev.*, 2014, **43**, 3957–3975.
- 48 Y. Xie, W. Chen, G. Bertoni, I. Kriegel, M. Xiong, N. Li, M. Prato, A. Riedinger, A. Sathya and L. Manna, *Chem. Mater.*, 2017, **29**, 1716–1723.
- 49 H. Yang, G. Li, J. W. Stansbury, X. Zhu, X. Wang and J. Nie, *ACS Appl. Mater. Interfaces*, 2016, **8**, 28047–28054.
- 50 M. He, Q. Wang, J. Zhang, W. Zhao and C. Zhao, *ACS Appl. Mater. Interfaces*, 2017, **9**, 44782–44791.
- 51 Y. Yuan, J. Liu and B. Liu, *Angew. Chem., Int. Ed.*, 2014, **53**, 7163–7168.
- 52 Y. Liu, M. Liu and M. T. Swihart, *Chem. Mater.*, 2017, **29**, 4783–4791.
- 53 Y. Xie, A. Riedinger, M. Prato, A. Casu, A. Genovese, P. Guardia, S. Sottini, C. Sangregorio, K. Miszta, S. Ghosh, T. Pellegrino and L. Manna, *J. Am. Chem. Soc.*, 2013, **135**, 17630–17637.
- 54 C. Wu, Y. Zhou, M. Xu, P. Han, L. Chen, J. Chang and Y. Xiao, *Biomaterials*, 2013, **34**, 422–433.
- 55 I. Burghardt, F. Lüthen, C. Prinz, B. Kreikemeyer, C. Zietz, H. G. Neumann and J. Rychly, *Biomaterials*, 2015, **44**, 36–44.
- 56 A. Gopal, V. Kant, A. Gopalakrishnan, S. K. Tandan and D. Kumer, *Eur. J. Pharmacol.*, 2014, **731**, 8–19.
- 57 J. Li, L. Tan, X. Liu, Z. Cui, X. Yang, K. W. K. Yeung, P. K. Chu and S. Wu, *ACS Nano*, 2017, **11**, 11250–11263.